Efficient Exciton Transport between Strongly Quantum-Confined Silicon Quantum Dots

Zhibin Lin,[†,*] Huashan Li,[†,*] Alberto Franceschetti,[‡,*] and Mark T. Lusk[†,*]

[†]Department of Physics, Colorado School of Mines, Golden, Colorado 80401, United States and [‡]National Renewable Energy Laboratory, Golden, Colorado 80401, United States

ABSTRACT

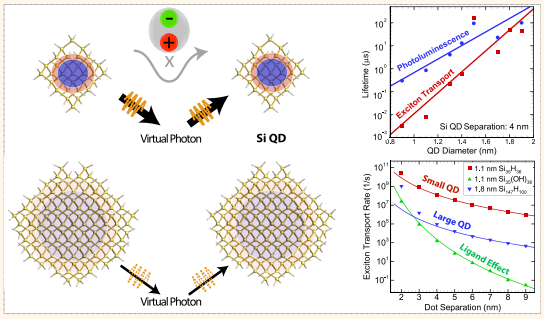

Many-body Green function analysis and first-order perturbation theory are used to quantify the influence of size, surface reconstruction, and surface treatment on exciton transport between small silicon quantum dots. Competing radiative processes are also considered in order to determine how exciton transport efficiency is influenced. The analysis shows that quantum confinement causes small (~1 nm) Si quantum dots to exhibit exciton transport efficiencies far exceeding that of their larger counterparts for the same center-to-center separation. This surprising result offers the prospect of designing assemblies of quantum dots through which excitons can travel for long distances, a game-changing paradigm shift for next-generation solar energy harvesting. We also find that surface reconstruction significantly influences the absorption cross section and leads to a large reduction in both transport rate and efficiency. Further, exciton transport efficiency is higher for hydrogen-passivated dots as compared with those terminated with more electronegative ligands, a result not predicted by Förster theory.

KEYWORDS: exciton transport · silicon quantum dots · photovoltaic · many-body theory · Fermi's golden rule

Recent advances in the synthesis of semiconductor quantum dots (QDs) have opened up an intriguing opportunity for exploiting quantum confinement to inexpensively improve photovoltaic energy conversion efficiency.[1−10] With tunable optical gaps and strong absorption cross sections, manufacture-friendly assemblies composed of QDs offer a design panacea for efficient exciton generation, but carrier transfer out of such materials is still problematic. Charge separation paradigms are being explored in which polymeric charge transport networks are interspersed with the QDs, but these are currently limited by the low efficiency of charge separation and carrier transport inherent with the polymers.[11,12] Recently though, Lu *et al.*[13,14] proposed an alternative paradigm in which nonradiative resonant exciton transfers occur between QDs in a PbS QD assembly and ultimately between the QDs and Si nanowires, in which the excitons dissociate into separate electrons and holes. Dorn *et al.*[15] also utilized exciton energy transfer from CdSe/CdS core/shell QDs to CdSe nanowires, which provide excellent charge transport, and they demonstrated an increase in photocurrent extraction from a QD solid by 2 to 3 orders of magnitude. As expected, this promising approach depends critically on the efficiency of such exciton transport as compared with competing relaxation mechanisms. This has motivated us to quantify the ways in which exciton transport efficiency can be optimized by varying the size, spacing, and surface termination of QDs.

We chose to study silicon-based QDs because they are environmentally benign, are inexpensive to fabricate, and have received a great deal of attention lately for photovoltaic and light-emitting diode applications.[16−18] For instance, carrier multiplication through multiple-exciton generation (MEG) has been recently demonstrated in colloidal silicon QDs[4] and for Si QDs embedded in a SiO_2 matrix.[5,7] This promise, though, has been somewhat shadowed by theoretical predictions[19] that resonant energy transfer between large (~2−4 nm) Si QDs is possible only when they are almost in contact because of the relative efficiency of radiative relaxation. We have therefore focused on small Si QDs with diameters of ~1−2 nm in the hopes of finding transport properties

* Address correspondence to zlin@mines.edu; huali@mines.edu; Alberto.Franceschetti@nrel.gov; mlusk@mines.edu.

Received for review January 23, 2012 and accepted April 2, 2012.

Published online April 02, 2012
10.1021/nn3003407

more conducive to technological applications. This small-size regime already offers advantages. Recent work has shown that MEG is more efficient in small QDs,[9,20] and the properties of such small dots are more easily tailored *via* surface termination.[21] In addition, dots of this size are less likely to have defects than their larger counterparts,[22] and there is a thermodynamic advantage to working with small QDs.[20]

Provided that the QDs are sufficiently well separated, exciton hopping can be considered within the framework of Förster resonance energy transfer (FRET), wherein Coulomb interactions are approximated using either dipole−dipole[23] or higher-order multipole expansions.[24] However, it is not clear that such approximations are appropriate, because Förster theory (FT) assumes a point dipole interaction, while QDs have a finite size. When nanometer-scale ligands are all that separate dots, the applicability of FT is particularly questionable.

Several recent theoretical studies have aimed to examine the validity of FT in semiconductor QDs. Curutchet *et al.*[25] examined the electronic coupling between two 3.9 nm CdSe QDs and also between a QD and a chlorophyll molecule. They found that the dipole approximation works rather well for spherical QDs even at contact separations. Schrier and Wang[26] studied the shape dependence of resonant energy transfer between CdSe QDs and found that the dipole−dipole interaction underestimates the coupling between linearly oriented nanorods and overestimates the coupling between parallel nanorods. Baer and Rabani[27] investigated the relative contribution of various multipole interactions to FRET. Allan and Delerue[19] studied the resonant energy transfer between QDs using a tight-binding approach and found that, for direct-gap InAs, the transfer rate is well described by FT. However, their results also showed that FT fails for Si QDs at small dot separations due to the weakness of dipolar transitions, a reflection of the indirect nature of the band gap in Si. This has motivated us to consider a many-body Green function approach that is not based on the assumption that dipole−dipole interactions dominate, a central tenant of FT.

RESULTS: EXCITON TRANSPORT BETWEEN HYDROGEN-PASSIVATED SI QDS

Figure 1a illustrates the exciton transport process between two identical Si QDs in this study. Eight different QD sizes were considered in this work: D = 0.9 nm ($Si_{17}H_{36}$), 1.1 nm ($Si_{35}H_{36}$), 1.3 nm ($Si_{66}H_{64}$), 1.4 nm ($Si_{78}H_{64}$), 1.5 nm ($Si_{87}H_{76}$), 1.7 nm ($Si_{123}H_{100}$), 1.8 nm ($Si_{147}H_{100}$), and 1.9 nm ($Si_{175}H_{116}$), where D is the QD diameter. To account for the quasiparticle effects and electron−hole interactions, a many-body Green function approach was employed to calculate the excitonic eigenstates in these quantum-confined

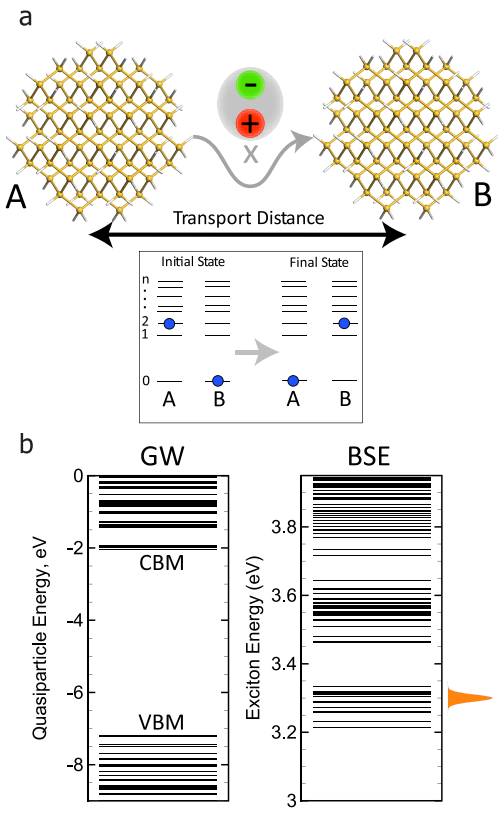

Figure 1. (a) Schematic diagram of an exciton, initially located on dot A, hopping to neighboring dot B with corresponding energy levels shown in the bottom panel. The ground state for a single QD is denoted by 0 in a Si QD with 1, 2, and *n* corresponding to lowest, second lowest, and *n*th excitonic states. Degenerate excitonic states may exist and are fully taken into account in the calculation of transport rates. (b) Quasiparticle energy levels from GW calculations and lowest exciton energy levels obtained by solving the Bethe−Salpeter equation for a 1.5 nm ($Si_{87}H_{76}$) Si QD. Thermal broadening of excitonic levels due to the electron−phonon coupling is represented by a Gaussian function with a width of 10 meV.

structures.[28−31] Figure 1b shows the quasiparticle energy levels from the GW calculation and lowest exciton energy levels from solving the Bethe−Salpeter equation (BSE) for a 1.5 nm ($Si_{87}H_{76}$) Si QD. Note that the BSE excitonic gap, 3.2 eV, is significantly smaller than the GW quasiparticle gap, 5.1 eV, because of strong electron−hole Coulomb interactions. The exciton transport rates were quantified using Fermi's golden rule:

$$\Gamma_{ET} = \frac{2\pi}{\hbar}\sum_{i,f} p(i)\,|\langle\Phi_i|\ W\ |\Phi_f\rangle|^2\delta(E_i - E_f) \qquad (1)$$

where Φ_i and Φ_f are the many-body electron wave functions for initial (i) and final (f) excitonic states. The term $p(i)$ accounts for the room-temperature Boltzmann occupation of the initial state. E_i and E_f are the energies of the initial and final excitonic states, and W is the screened Coulomb interaction. Energy conservation during the exciton transport process is enforced by replacing the delta function of eq 1 with a Gaussian profile that has a variance of 10 meV. This accounts for

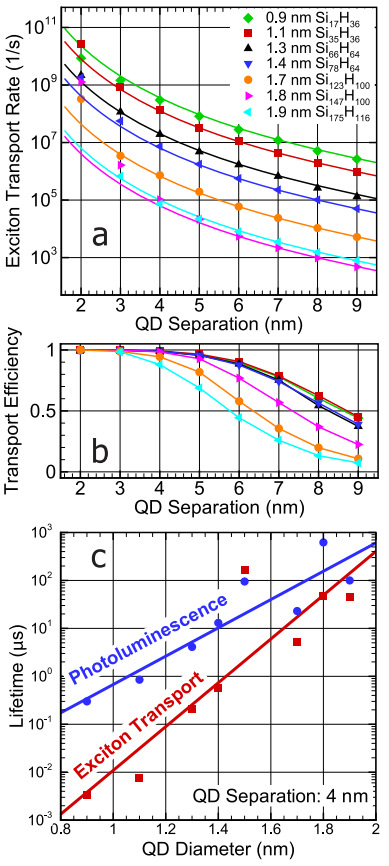

Figure 2. Exciton transport rate (a) and efficiency (b) as a function of dot center separation in seven hydrogen-passivated Si QDs: 0.9 nm ($Si_{17}H_{36}$) 1.1 nm ($Si_{35}H_{36}$), 1.3 nm ($Si_{66}H_{64}$), 1.4 nm ($Si_{78}H_{64}$), 1.7 nm ($Si_{123}H_{100}$), 1.8 nm ($Si_{147}H_{100}$), and 1.9 nm ($Si_{175}H_{116}$). Solid curves in panel (a) are obtained directly from dipole matrix elements between excitonic states and the ground state within Förster theory wherein transport rates scale as $1/R^6$ (eq 7). Plot in panel (b) is exciton transport efficiency, defined as the ratio of exciton transport rate and total exciton decay rate. Solid lines in panel (b) are guides to the eye. Lifetimes for photoluminescence and exciton transport at 4 nm QD separation are plotted as a function of dot diamter in panel (c). Solid lines in (c) are fitted to the data.

the thermal broadening effects of excitonic levels due to electron–phonon coupling in Si QDs.[19,32]

Figure 2a shows the exciton transport rates, Γ_{ET}, in seven hydrogen-passivated Si QDs for a range of center-to-center separations. The results show that, for a wide range of center-to-center separations, the rate of exciton transport *generally* increases as the dot size decreases. Moreover, these rates increase rapidly as the center-to-center distance decreases. Since the exciton mobility scales as the ratio of the square of hopping distance per hopping time, this better than logarithmic increase implies that the highest mobility is achieved by making dots as small and as close together as possible. The increase in transport rate with decreasing dot size is due to the effect of quantum confinement on the intradot oscillator strengths. As shown by Dexter,[24] within the dipole–dipole approximation the direct Coulomb interactions can be represented as the product of intradot oscillator strengths of initial and final excitons. As the dot size decreases, the oscillator strength in small Si QDs increases drastically,[36,37] leading to the strong enhancement in the exciton transport rates.

The results of our calculations also show that FT breaks down for dots separated by less than 2 nm (Figure 2a). This deviation is due to the influence of higher-order multipole interactions, which are missing from FT. At large distances, though, the calculated exciton transport rates are well described by the $1/R^6$ scaling of FT quantified using the results obtained from our GW-BSE calculations (see Methods section). Even this region of correspondence may seem surprising since the dipole interactions underlying FT are zero for indirect gap materials as a result of momentum conservation. However, quantum confinement is very significant for the small QDs considered here, and materials thus constrained have a pseudodirect dipolar transition.[19,37−40] In addition to this observation, it is noted that at a short distance of 2 nm the smallest 0.9 nm dot has a slightly smaller transport rate than a 1.1 nm dot, opposite of the trend predicted from higher-order multipole interactions. This suggests that the specific orientation of the small dot becomes important at close dot separations and the assumption of spherical geometry of the dot in FT at these distances might fail.

To further check the influence of the orientation of the QD on the exciton transport rates, we carried out the same analysis for two 0.9 nm dots aligned in the [011] direction instead of the [001] direction. It was found that, at 2 nm, the exciton transport rate increases by an order of magnitude over the results shown in Figure 2a. As the QD separation increases, however, the difference between the transport rates for these two orientations becomes much smaller, and for distances larger than 4 nm the transport rates for both orientations follow the same FT curve.

When the surfaces of two dots are in close vicinity, exchange interactions could become comparable with direct Coulomb interactions due to strong Pauli exclusion. Therefore the transport rates at short distances will depend on the specific location and orientation of the QDs and should be calculated from a full calculation using eq 1, as done in this study. The application of FT at such conditions might yield inaccurate results, as shown in Figure 2a. This is made clear by comparing the Figure 2a transport rates for 1.7 and 1.8 nm dots; the more accurate analysis shows that the larger dot actually has a higher transport rate for separations less than 2 nm, but this transition is not predicted by FT.

While the above trends in transport *rate* are significant on their own, they do not necessarily translate into gains in transport *efficiency*. In particular, photoluminescence (PL) rate is also influenced by QD size, separation, and terminating structure. In order to

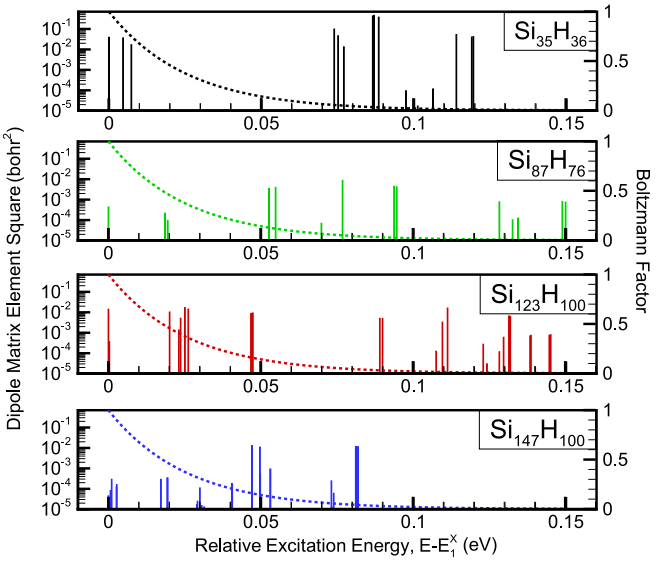

Figure 3. Dipole matrix element squares and room-temperature Boltzmann factors (dashed lines), $e^{-(E^X-E^X_1)}/k_BT$, of excitonic states for four hydrogen-terminated Si QDs. Excitonic energies, E^X, are shown with respect to the energy of lowest excitonic state, E^X_1, in corresponding QDs.

quantify how transport rates change relative to the rate of exciton recombination, we define a radiatively limited *exciton transport efficiency*, $p = \Gamma_{ET}/(\Gamma_{ET} + \Gamma_{PL})$, where Γ_{PL} is the room-temperature PL rate defined as[42,43]

$$\Gamma_{PL} = \frac{1}{\tau_{PL}} = \sum_i p(i)\frac{4e^2 f_1^{\,2}(\varepsilon_{QD})E_i^{\,3}}{3c^3\hbar^3}\,|M_i\,|^2 \qquad (2)$$

Here τ_{PL} is the average PL lifetime calculated from the oscillator strengths of the excitonic states, E_i is the excitonic energy of excited state i, f_1 is the local field factor derived from the effective dielectric constant (see Methods section), and M_i is the dipole matrix element between excitonic state i and the ground state.

This measure of transport efficiency is provided in Figure 2b for seven hydrogen-passivated Si QDs. For dot separations of less than 3 nm, the transport efficiencies for all seven dot sizes are nearly identical and are greater than 0.95. This makes sense since the transport rates at these distances are much larger, sometimes by several orders of magnitude, than the associated PL rates. Within this regime, for instance, it is more probable for 13 exciton jumps to occur than for the exciton to recombine radiatively. The transport efficiency between the three smallest dots, though, remains greater than 50% out to separations of 8 nm, *i.e.*, at more than 6 times the dot diameters. Furthermore the transport efficiency exhibits an asymptote for dots approaching 1 nm in diameter and indicates a target design range closer to 1 nm than 2 nm.

The reason that the transport efficiency increases as dot size decreases can be explained using the dipole–dipole approximation, where exciton transport can be viewed as a two-step process of photon emission and absorption.[19] Expressed in terms of effective emission and absorption cross sections, $\bar{\sigma}_e$ and $\bar{\sigma}_a$, the transport efficiency can be expressed as

$$p = \frac{c_X\bar{\sigma}_e\bar{\sigma}_a}{c_X\bar{\sigma}_e\bar{\sigma}_a + c_{PL}\bar{\sigma}_e} \qquad (3)$$

The effective emission cross section appears in both rate expressions and so falls out of the transport efficiency expression. The efficiency is therefore determined by the effective absorption cross section, which generally increases as dot size decreases due to quantum confinement. This is consistent with the results shown in Figure 2b. As a check of this argument, Figure 2c shows the lifetimes for PL and exciton transport at 4 nm QD separation for all eight hydrogen-passivated Si QDs in this study. The ratio of the slopes fitted to the exciton transport and PL lifetimes is found to be about 1.5, suggesting that the exciton transport rate scales roughly as the square of the PL rate. This is consistent with the two-step picture of virtual photon emission and absorption in the exciton transport process at large dot separations.

Consistent with the results of Figure 2, there is a general trend associated with the dipole matrix elements of the lowest excitonic states. In particular, these elements tend to increase rapidly as the dot size decreases due to quantum confinement. Our many-body Green function analysis shows, though, that the dipole matrix elements exhibit a distribution of strengths at low excitation energy levels, Figure 3, that is extremely sensitive to QD geometry and cannot be described as a monotonic correlation with dot size. This is very significant to exciton transport since these are the states that are thermally occupied at room

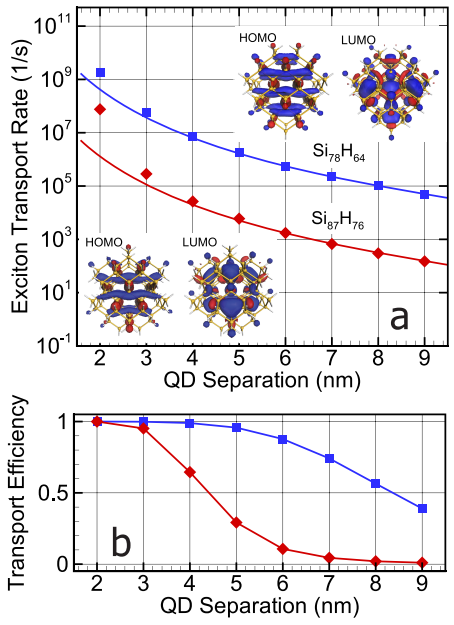

Figure 4. Exciton transport rate (a) and efficiency (b) as a function of dot center separation for 1.4 nm ($Si_{78}H_{64}$) and 1.5 nm ($Si_{87}H_{76}$) Si QDs. HOMO and LUMO wave functions of both dots are shown in the insets, in which the blue color corresponds to positive and red to negative isovalues. Solid curves in (a) are obtained in the same way as described in Figure 2a, and solid lines in (b) are guides to the eye.

temperature, as shown by the Boltzmann factors in Figure 3. These dipole matrix elements, in turn, define the strengths of both PL and exciton transport processes in Figure 2.

This is made particularly clear by considering quantum dots that maintain a T_d symmetry but exhibit noncompact structures. For instance, the slight waist of $Si_{87}H_{76}$ (1.5 nm), shown in the inset of Figure 4, results in very small oscillator strengths and transport rates much lower than a compact dot of approximately the same size, $Si_{78}H_{64}$ (1.4 nm). In fact, the $Si_{87}H_{76}$ dot has transport rates lower than most of the dots considered in our study. Figure 4 shows that these two dots have significantly different LUMO wave functions with the $Si_{87}H_{76}$ distribution pushed away from its center due to the midregion waist. This structural sensitivity of exciton transport suggests that it might be possible to structurally engineer geometries for optimized transport efficiency.

Si QDs may undergo surface reconstruction in environments with low hydrogen levels, and this influences the exciton transport efficiency. In particular, 2×1-like surface reconstruction can occur on the (100) facets of Si QDs, reducing the number of surface dangling bonds and thus resulting in lower hydrogen coverage on the dot surface. To analyze the impact of such reconstructions, we compared the transport efficiencies of a reconstructed $Si_{66}H_{40}$ dot with their unreconstructed $Si_{66}H_{64}$ counterparts. Figure 5a and b show that surface reconstruction leads to a reduction

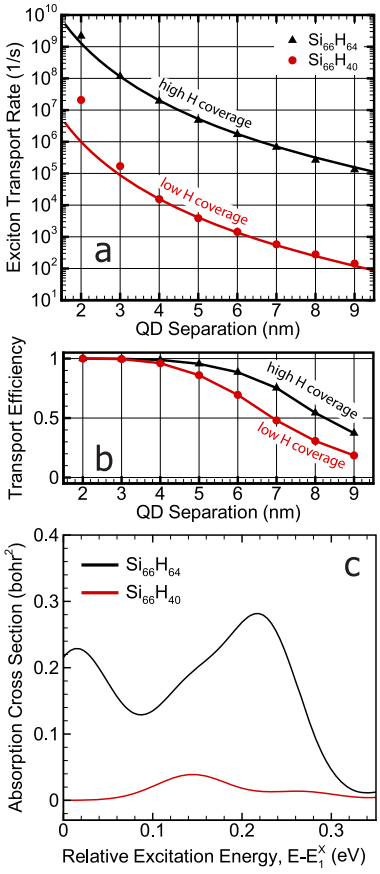

Figure 5. (a) Exciton transport rate, (b) efficiency, and (c) absorption cross section in unreconstructed (high H coverage) $Si_{66}H_{64}$ and reconstructed (low H coverage) $Si_{66}H_{40}$ QDs. Excitation energies are shown with respect to the energy of lowest excitonic state, E_1^X, in corresponding QDs. Solid curves in (a) are obtained in the same way as described in Figure 2a, and solid lines in (b) are guides to the eye. The dipole matrix element squares for lowest excitonic states of $Si_{66}H_{64}$ and $Si_{66}H_{40}$ are 2.4×10^{-2} and 1.2×10^{-6} (in au), respectively.

in both the exciton transport rate and efficiency. This is due to the fact that surface reconstruction significantly reduces the oscillator strengths, as depicted in Figure 5c from GW-BSE calculations. The reduction, in turn, is due to the redistribution of electronic wave functions in response to surface strain generated by surface reconstruction. The behavior is similar to that caused by an increase in QD size (Figure 2a); that is, both surface reconstruction and an increase in dot size decrease the oscillator strengths of the lowest excitonic states. These excitonic states are heavily involved in exciton transport due to the large probability of occupying these states at room temperature according to a Boltzmann distribution.

RESULTS: INFLUENCE OF SURFACE PASSIVANTS ON EXCITON TRANSPORT

The influence of surface treatment on exciton transport rate was investigated using Si_{35} QDs passivated with five different ligands, H, CH_3, F, Cl, and OH, and the

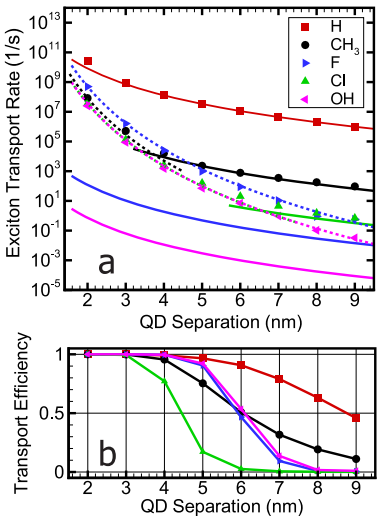

Figure 6. Exciton transport (a) rate and (b) efficiency in 1.1 nm Si_{35} QDs with different surface terminations. Five surface passivants were considered: H, CH_3, F, Cl, and OH. In (a), solid curves showing a $1/R^6$ scaling of FT are obtained in the same way as described in Figure 2a, while dashed curves show $1/R^{14}$ fit to the transport rates from CH_3, F, Cl, and OH passivants. Solid lines in panel (b) are guides to the eye.

results are summarized in Figure 6. Earlier calculations for OH passivation using density-functional theory (DFT) with a B3LYP exchange/correlation functional found that the HOMO−LUMO transition is dipole forbidden.[41] Consistent with this, we have found that the symmetry of the HOMO level changes from T_2 to T_1 after substituting H with OH ligands, creating a forbidden transition between HOMO and LUMO (A1). However, our approach explicitly takes many-body and excitonic effects into account, and the result of mixing with other dipole-allowed transitions makes the lowest excitonic state weakly allowed; that is, there is a nonzero oscillator strength. The significant drop in exciton transport rate that results from passivation with OH instead of H (Figure 6) is directly related to much weaker oscillator strengths for the lowest excitonic states in OH-passivated Si QDs. The influence of the more electronegative OH passivants on the surface leads to a redistribution of the wave functions toward the surface. We found that for all four passivations other than H, the HOMO wave function is more affected by the change of surface ligands than the LUMO wave function. For instance, more than 20% of HOMO wave function density originally located near the dot center of $Si_{35}(H)_{36}$ moves out to the surface region in $Si_{35}(OH)_{36}$, whereas the LUMO in $Si_{35}(OH)_{36}$ exhibits a very similar radial distribution to the one with H passivation. The effect of OH passivation on the oscillator strengths for optical transitions might be related to previous experimental observations of a long, 10^{-3} s, PL lifetime for 1 to 2 nm Si QDs with an oxide shell.[44,45] The same symmetry change in the HOMO orbital also occurs with the three other terminating groups considered: CH_3, F, and Cl. As a result, the dipole transitions between HOMO and LUMO orbitals for these QDs are very weak, leading to much smaller exciton transport rates shown in the top panel (a) of Figure 6.

Figure 6a further indicates that the exciton transport rates for F- and OH-passivated Si QDs exhibit a strong $1/R^{14}$ dependence, and this is also true for CH_3 and Cl passivation at small dot separation (less than 4 nm). This scaling relationship suggests that, for F- and OH-passivated Si QDs, the leading term in the multipole expansion of the Coulomb interaction is an octupole−octupole interaction; quadrupole interactions vanish due to the T_d symmetry of the QD structure. Nevertheless, the octupole−octupole interaction still dominates the range of dot separation considered in this study, and FT gives an incorrect prediction of exciton transport rates at all distances. The same conclusions apply to dots passivated with CH_3 and Cl, in which the $1/R^6$ scaling of FT begins to take over only at dot separations of approximately 4 and 9 nm, respectively. For CH_3 passivation, even though the lowest excitonic state has a very weak oscillator strength due to dipole-forbidden HOMO−LUMO transition, the next excitonic states (only ∼180 meV higher) have oscillator strengths that are approximately 6 orders of magnitude higher. As a result, beyond 4 nm (Figure 6a), where the octupole−octupole interactions become weak, the exciton transport rates exhibit the $1/R^6$ trend as predicted from a dipole−dipole approximation.

We now turn our attention to the influence of surface termination on transport efficiency, with our analysis summarized in Figure 6b. The efficiency is nearly unity for all five passivations when the dots are separated by less than 3 nm. At larger distances, though, the H-passivated dots exhibit a much higher transport efficiency. On the other hand, dots passivated with more electronegative F, Cl, and OH give rise to longer averaged PL lifetimes, potentially increasing the time window for excitons to be transported. However, the Γ_{PL}/Γ_{ET} ratio for these passivations still remains much larger than that for H passivation. This leads to less efficient exciton transport for Si QDs terminated with these passivants. Nevertheless, for F- and OH-passivated Si QDs, long PL lifetimes in the lowest exciton states due to weak dipole moments still result in a relatively high transport efficiency at dot separations less than 5 nm. For CH_3, the lowest excitonic energy is found to be about 4.2 eV, very close to that of H-passivated Si_{35}, and its PL lifetime is much longer (2×10^{-3} s) than that for H termination (8.5×10^{-7} s). Due to relatively weak exciton transport rates, CH_3 passivation exhibits a lower transport efficiency than that of H termination.

The impact of ligand substitution on exciton transport was further investigated by varying the surface

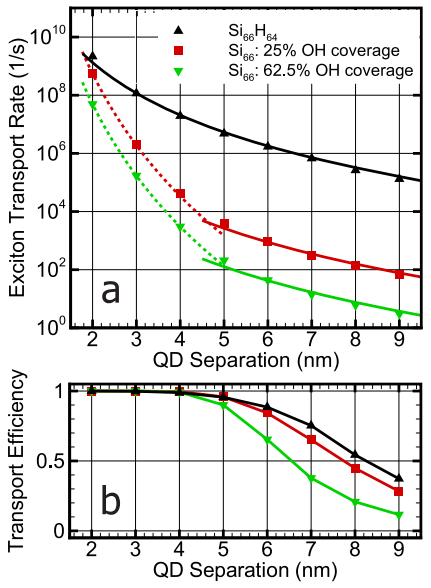

Figure 7. Exciton transport (a) rate and (b) efficiency in 1.3 nm Si_{66} QDs with different surface coverage of OH ligands, namely, 0% ($Si_{66}H_{64}$), 25%, and 62.5% surface coverage. In (a), solid curves showing a $1/R^6$ scaling of FT are obtained in the same way as described in Figure 2a, while dashed curves show a $1/R^{14}$ fit to the transport rates of 25% and 62.5% OH coverage for QD separations below 4 nm. Solid lines in panel (b) are guides to the eye.

coverage of OH. We calculated the exciton transport rate and efficiency for Si_{66} QDs with 25% and 62.5% surface coverage of OH and compared the results with $Si_{66}H_{64}$. In the partial OH passivation, hydrogen atoms are substituted with OH ligands to create partial coverage of OH on the QD surface. Note that full coverage of OH ligands on Si_{66} is hindered by the steric effects of the passivants on the surface. The effect of replacing hydrogen passivation with OH on exciton transport can be clearly seen in Figure 7. The exciton transport rates for Si_{66} QDs with 25% and 62.5% surface coverage of OH exhibit $1/R^{14}$ scaling for dot center separations below 4 nm and $1/R^6$ beyond 4 nm. For $Si_{66}H_{64}$ with 0% OH coverage, the transport rates follow the $1/R^6$ scaling for separations greater than 2 nm. As discussed earlier, the redistribution of electron wave functions to the surface region due to the more electronegative OH on the dot surface could result in vanishing dipole moments between the orbitals. As the OH coverage on the QD surface is increased, the exciton transport rate decreases for all QD separations. The exciton transport efficiency (Figure 7b) is nearly unity at QD separations less than 4 nm for all three OH coverages due to the much faster exciton transport rates as compared to the PL rates in the dots. The influence of surface coverage of OH ligands on the transport efficiency, however, becomes apparent at large dot separation, as increasing OH coverage results in significantly lower transport efficiency. A distortion of the associated wave functions, due to ligand substitution, is shown to be the cause of the significant changes to the exciton transport rate and efficiency.

TABLE 1. Lowest Singlet Excitonic Energy, E_1^X, Exciton Binding Energy, E_b, Room-Temperature PL Lifetime, τ_{PL}, and Effective Dielectric Constant, ε_{QD}, for Nine Hydrogen-Passivated Si QDs in This Study

QD	diameter, nm	E_1^X, eV	E_b, eV	τ_{PL}, s	ε_{QD}
$Si_{17}H_{36}$	0.9	4.8	3.5	3.0×10^{-7}	1.12
$Si_{35}H_{36}$	1.1	4.1	2.8	8.5×10^{-7}	1.15
$Si_{66}H_{64}$	1.3	3.7	2.3	4.1×10^{-6}	1.20
$Si_{66}H_{40}$	1.3	2.5	2.2	1.5×10^{-3}	1.12
$Si_{78}H_{64}$	1.4	3.6	2.2	1.3×10^{-5}	1.23
$Si_{87}H_{76}$	1.5	3.2	2.0	9.5×10^{-5}	1.27
$Si_{123}H_{100}$	1.7	3.0	1.9	2.3×10^{-5}	1.35
$Si_{147}H_{100}$	1.8	3.0	1.7	6.2×10^{-4}	1.34
$Si_{175}H_{116}$	1.9	2.7	1.6	1.0×10^{-4}	1.39

CONCLUDING REMARKS

Exciton transport in ~1−2 nm Si nanocrystalline QDs has been investigated using an *ab initio* many-body approach. Within first-order perturbation theory, we have found that small (~1 nm) hydrogen-terminated Si QDs exhibit highly efficient exciton transport as a result of strong quantum confinement. We also show that surface reconstruction significantly reduces exciton transport efficiency. Our findings suggest that small Si QDs, of size about 1 nm, should exhibit the highest exciton transport process, potentially facilitating the photoconversion process in Si QD assemblies for an improved photovoltaic efficiency. In particular, we predict that exciton transport should be the most efficient for hydrogen-terminated Si QDs of size less than 1.5 nm in diameter. The transport distance for these small Si QDs could be much larger than the typical dot size; for example, the transport efficiency still exceeds 0.5 with an 8 nm separation between dot centers. We also examined several other surface terminations, including CH_3, F, Cl, and OH, in Si QDs and found that, at the same QD separation, exciton transport is more efficient in H-terminated Si QDs than QDs passivated with the other types of surface ligands.

For small hydrogen-terminated Si QDs, Förster's $1/R^6$ expression agrees very well with exciton transport rates calculated from first principles except at short distances (~2 nm), where multipole interactions become important. For other surface passivations (F, Cl, and OH), though, Förster's theory fails to predict correct exciton transport rates due to the vanishing dipole moments in these structures. Exciton transport in F- and OH-passivated Si QDs is dominated by octupole−octupole interactions, and the associated long PL lifetime is due to weak dipole matrix elements. This results in a relatively high transport efficiency for dot separations of less than 5 nm.

It should be noted that a monodisperse QD distribution is assumed in this study since only exciton transport between two identical QDs is considered. In a polydisperse QD ensemble, it is possible that excitons could be trapped in larger QDs in which the electron and hole would eventually recombine. The sensitivity of such exciton trapping to a given size distribution needs to be carefully considered. In any case, it might be possible to construct a QD solar-cell architecture in which layers of small QDs at the top (sun side) are followed by layers of larger QDs, with the largest ones at the bottom in contact with a substrate that would promote exciton dissociation and charge transport.[13−15]

METHODS

All Si QD geometries were optimized within a local density approximation using standard DFT. The influence on exciton dynamics of five terminating ligands was considered: H, CH_3, F, Cl, and OH. A many-body Green function approach, explicitly accounting for the quasiparticle effects and electron−hole interactions, was then employed to calculate the excitonic eigenstates in these quantum-confined structures. In particular, the electron self-energy was calculated within the GW_f approximation,[28,29] and excitonic effects were accounted for by solving the Bethe−Salpeter equation.[28,30,31] The GW-BSE calculations were carried out using real-space implementation of density-functional theory (PARSEC)[46,47] and many-body Green function approach (RGWBS).[28,48] The lowest excitonic energies obtained in our calculations (Table 1) agree well with earlier GW-BSE calculations.[28]

Within first-order perturbation theory, the exciton transport rates are quantified using Fermi's golden rule, eq 1, which takes into account both direct and exchange Coulomb interactions between the initial and final states as well as the screening of the Coulomb interactions due to other excitonic states. A complete account of screening was not undertaken in this study because of the computational demands associated with the mixing of the large number of excitonic states. Instead, we used local field factors[19,27] to approximate the screening of interdot Coulomb interactions. The approach serves as an approximate means of extending the validity of a multipole expansion of the Coulomb operator down to the length scales of interest in the current setting. These field factors, in turn, are based on the notion of an effective dielectric constant, ε, defined as the ratio of unscreened and screened Coulomb energies of the lowest triplet excitonic state from GW-BSE calculations. The effective dielectric constants for all Si dots considered in this work (Table 1) were found to be small, less than 2, as compared to a value of 11.4 for bulk silicon.[33] In addition, exciton binding energies for the small Si QDs in this study range from 1.6 eV (D = 1.9 nm) to 3.5 eV (D = 0.9 nm). The large exciton binding energies are a direct consequence of strong quantum confinement effects and weak dielectric screening of electron−hole Coulomb interactions in these small Si dots. These are consistent with previous calculations for Si QDs of similar sizes.[35]

The effective dielectric constant can be used to approximate the Coulomb integral of eq 1 by modifying a standard multipole expansion so that each term has a local field factor, f_l, that accounts for the effective interdot screening of the lth multipole:[27]

$$f_l(x) = \frac{2l+1}{(x+1)l+1} \tag{4}$$

Here $x = \varepsilon_{QD}/\varepsilon_0$, where ε_{QD} and ε_0 are the effective dielectric constants of the QD and medium, respectively; we assume vacuum conditions outside of the QDs so that $\varepsilon_0 = 1$. Then the field factor corresponding to the case of two identical QDs under the dipole−dipole approximation is $f_1(\varepsilon_{QD}) = 3/(\varepsilon_{QD} + 2)$.

A further simplification can be made because, for the weak dielectric screenings considered in this work (Table 1), the differences between field factors for poles of different orders are small. We therefore dropped the order dependence and assumed $f_l(\varepsilon_{QD}) \approx f_1(\varepsilon_{QD})$, corresponding to the case of two identical QDs under the dipole−dipole approximation. With an approximation for the interdot screening now in hand, the multipole expansion can then be collapsed back into a bare Coulomb integral. The standard representation of this integral in terms of the orbitals of two Slater determinants[34] can be used to rewrite eq 1:

$$\Gamma_{ET} = \frac{2\pi}{\hbar}\left(\frac{3}{\varepsilon_{QD}+2}\right)^4 \sum_{i,f} p(i)\,|\sum_{j,k} B_j^i B_k^f (K_{c_j^A, v_j^A, v_k^B, c_k^B} - K_{c_j^B, c_k^B, v_k^B, v_j^A})\,|^2 \delta(E_i - E_f) \tag{5}$$

The first and second term appearing inside the parentheses of eq 5 are the bare direct and exchange Coulomb integrals defined as[34]

$$K_{m,n,p,q} = \sum_{\sigma,\sigma'} \int\int \mathrm{d}r\,\mathrm{d}r'\,\psi_m^*(r,\sigma)\,\psi_n(r,\sigma)\frac{e^2}{|r-r'|}\psi_p^*(r',\sigma')\,\psi_q(r',\sigma') \tag{6}$$

The coefficients, B_j^i and B_k^f appearing in eq 5 are the BSE eigenvectors for the exciton configuration j (constructed from single-particle valence orbital ψ_j^v and single-particle conduction orbital ψ_j^c on dot A) of the initial state and the exciton configuration k (ψ_k^v and ψ_k^c on dot B) of the final state, respectively.[28] For the range of dot separations considered in this study, we find that the contribution of the exchange Coulomb interaction to the exciton transport rates is negligible except when the dots are very close to each other. At the shortest dot center separation considered in this study, 2 nm, the exchange Coulomb energies for 1.1 nm Si QDs are found to be more than 7 orders of magnitude smaller than the direct Coulomb energies. However for 1.9 nm Si QDs at 2 nm dot center separation the ratio between exchange and direct Coulomb energies increases to about 1:6 due to a much closer dot surface separation. Our calculations for exciton transport rates take into full account the exchange Coulomb interactions shown in eq 5 for all the dot separations.

On the other hand, within the dipole−dipole approximation the exciton transport rate in eq 1 can be expressed in terms of the dipole matrix elements of initial and final excitons during the transitions:[19]

$$\Gamma_{FT} = \frac{4\pi}{3\hbar}\frac{e^4}{R^6}\left(\frac{3}{\varepsilon_{QD}+2}\right)^4 \sum_{i,f} p(i)\,|M_i|^2\,|M_f|^2 \delta(E_i - E_f) \tag{7}$$

where R is the dot center-to-center separation and M_i and M_f are the dipole matrix elements between the excitonic state, i and f, and the ground state, respectively.

Conflict of Interest: The authors declare no competing financial interest.

Acknowledgment. This work was supported by the Renewable Energy Materials Research Science and Engineering Center (NSF grant no. DMR-0820518) at the Colorado School of Mines and the National Renewable Energy Laboratory. The calculations were carried out using the high-performance computing resources provided by the Golden Energy Computing Organization at the Colorado School of Mines (NSF grant no. CNS-0722415).

REFERENCES AND NOTES

1. Alivisatos, A. P. Semiconductor Clusters, Nanocrystals, and Quantum Dots. *Science* **1996**, *271*, 933–937.
2. Nozik, A. J. Quantum Dot Solar Cells. *Phys. E (Amsterdam, Neth.)* **2002**, *14*, 115–120.
3. Jurbergs, D.; Rogojina, E.; Mangolini, L.; Kortshagen, U. Silicon Nanocrystals with Ensemble Quantum Yields Exceeding 60%. *Appl. Phys. Lett.* **2006**, *88*, 233116.
4. Beard, M. C.; Knutsen, K. P.; Yu, P.; Luther, J. M.; Song, Q.; Metzger, W. K.; Ellingson, R. J.; Nozik, A. J. Multiple Exciton Generation in Colloidal Silicon Nanocrystals. *Nano Lett.* **2007**, *7*, 2506–2512.
5. Timmerman, D.; Izeddin, I.; Stallinga, P.; Yassievich, I. N.; Gregorkiewicz, T. Space-Separated Quantum Cutting with Silicon Nanocrystals for Photovoltaic Applications. *Nat. Photonics* **2008**, *2*, 105–109.
6. Madrid, A. B.; Hyeon-Deuk, K.; Habenicht, B. F.; Prezhdo, O. V. Phonon-Induced Dephasing of Excitons in Semiconductor Quantum Dots: Multiple Exciton Generation, Fission, and Luminescence. *ACS Nano* **2009**, *3*, 2487–2494.
7. Timmerman, D.; Valenta, J.; Dohnalova, K; de Boer, W. D. A. M; Gregorkiewicz, T. Step-like Enhancement of Luminescence Quantum Yield of Silicon Nanocrystals. *Nat. Nanotechnol.* **2011**, *6*, 710–713.
8. Nozik, A. J. Nanoscience and Nanostructures for Photovoltaics and Solar Fuels. *Nano Lett.* **2010**, *10*, 2735–2741.
9. Lin, Z.; Franceschetti, A.; Lusk, M. T. Size Dependence of the Multiple Exciton Generation Rate in CdSe Quantum Dots. *ACS Nano* **2011**, *5*, 2503–2511.
10. Hyeon-Deuk, K.; Prezhdo, O. V. Multiple Exciton Generation and Recombination Dynamics in Small Si and CdSe Quantum Dots: An *Ab Initio* Time-Domain Study. *ACS Nano* **2012**, *6*, 1239–1250.
11. Yu, G.; Heeger, A. J. Charge Separation and Photovoltaic Conversion in Polymer Composites with Internal Donor/Acceptor Heterojunctions. *J. Appl. Phys.* **1995**, *78*, 4510–4515.
12. Dittmer, J. J.; Marseglia, E. A.; Friend, R. H. Electron Trapping in Dye/Polymer Blend Photovoltaic Cells. *Adv. Mater.* **2000**, *12*, 1270–1274.
13. Lu, S.; Madhukar, A. Nonradiative Resonant Excitation Transfer from Nanocrystal Quantum Dots to Adjacent Quantum Channels. *Nano Lett.* **2007**, *7*, 3443–3451.
14. Lu, S.; Lingley, Z.; Asano, T.; Harris, D.; Barwicz, T.; Guha, S.; Madhukar, A. Photocurrent Induced by Nonradiative Energy Transfer from Nanocrystal Quantum Dots to Adjacent Silicon Nanowire Conducting Channels: Toward a New Solar Cell Paradigm. *Nano Lett.* **2009**, *9*, 4548–4552.
15. Dorn, A.; Strasfeld, D. B.; Harris, D. K.; Han, H.-S.; Bawendi, M. G. Using Nanowires To Extract Excitons from a Nanocrystal Solid. *ACS Nano* **2012**, *5*, 9028–9033.
16. Lu, Z. H.; Lockwood, D. J.; Baribeau, J. M. Quantum Confinement and Light Emission in SiO_2/Si Superlattices. *Nature* **1995**, *378*, 258–260.
17. Cheng, K.-Y.; Anthony, R.; Kortshagen, U. W.; Holmes, R. J. Hybrid Silicon Nanocrystal-Organic Light-Emitting Devices for Infrared Electroluminescence. *Nano Lett.* **2010**, *10*, 1154–1157.
18. Puzzo, D. P.; Henderson, E. J.; Helander, M. G.; Wang, Z.; Ozin, Z. G.; Lu, Z. Visible Colloidal Nanocrystal Silicon Light-Emitting Diode. *Nano Lett.* **2011**, *11*, 1585–1590.
19. Allan, G.; Delerue, C. Energy transfer between semiconductor nanocrystals: Validity of Forster's Theory. *Phys. Rev. B* **2007**, *75*, 195311.
20. Beard, M. C.; Midgett, A. G.; Hanna, M. C.; Luther, J. M.; Hughes, B. K.; Nozik, A. J. Comparing Multiple Exciton Generation in Quantum Dots To Impact Ionization in Bulk Semiconductors: Implications for Enhancement of Solar Energy Conversion. *Nano Lett.* **2010**, *10*, 3019–3027.
21. Kšnig, D.; James Rudd, J.; Green, M. A.; Conibeer, G. Role of the Interface for the Electronic Structure of Si Quantum Dots. *Phys. Rev. B* **2008**, *78*, 035339.
22. Niesar, S.; Stegner, A. R.; Pereira, R. N.; Hoeb, M.; Wiggers, H.; Brandt, M. S.; Stutzmann, M. Defect Reduction in Silicon Nanoparticles by Low-Temperature Vacuum Annealing. *Appl. Phys. Lett.* **2010**, *96*, 193112.
23. Förster, T. Zwischenmolekulare Energiewanderung und Fluoreszenz. *Ann. Phys.* **1948**, *2*, 55–75.
24. Dexter, D. L. A Theory of Sensitized Luminescence in Solids. *J. Chem. Phys.* **1953**, *21*, 836.
25. Curutchet, C.; Franceschetti, A.; Zunger, A.; Scholes, G. D. Examining Forster Energy Transfer for Semiconductor Nanocrystalline Quantum Dot Donors and Acceptors. *J. Phys. Chem. C* **2008**, *112*, 13336–13341.
26. Schrier, J.; Wang, L.-W. Shape Dependence of Resonant Energy Transfer between Semiconductor Nanocrystals. *J. Phys. Chem. C* **2008**, *112*, 11158–11161.
27. Baer, R.; Rabani, E. Theory of Resonance Energy Transfer Involving Nanocrystals: the Role of High Multipoles. *J. Chem. Phys.* **2008**, *128*, 184710.
28. Tiago, M. L.; Chelikowsky, J. R. Optical Excitations in Organic Molecules, Clusters, and Defects Studied by First-Principles Green's Function Methods. *Phys. Rev. B* **2006**, *73*, 205334.
29. Hybertsen, M. S.; Louie, S. G. Electron Correlation in Semiconductors and Insulators: Band Gaps and Quasiparticle Energies. *Phys. Rev. B* **1986**, *34*, 5390.
30. Onida, G.; Reining, L.; Rubio, A. Electronic Excitations: Density-Functional *versus* Many-Body Green's-Function Approaches. *Rev. Mod. Phys.* **2002**, *74*, 601–659.
31. Rohlfing, M.; Louie, S. G. Electron-Hole Excitations and Optical Spectra from First Principles. *Phys. Rev. B* **2000**, *62*, 4927–4944.
32. Delerue, C.; Lannoo, M. *Nanostructures: Theory and Modelling*; Springer-Verlag: Berlin, 2004.
33. Faulkner, R. A. Higher Donor Excited States for Prolate-Spheroid Conduction Bands: A Reevaluation of Silicon and Germanium. *Phys. Rev.* **1969**, *184*, 713–721.
34. Szabo, A.; Ostlund, N. *Modern Quantum Chemistry: Introduction to Advanced Electronic Structure Theory*; Dover, 1996.
35. Öğüt, S; Burdick, R; Saad, Y; Chelikowsky, J. R. *Ab Initio* Calculations for Large Dielectric Matrices of Confined Systems. *Phys. Rev. Lett.* **2003**, *90*, 127401.
36. Trani, F.; Cantele, G.; Ninno, D.; Iadonisi, G. Tight-Binding Calculation of the Optical Absorption Cross Section of Spherical and Ellipsoidal Silicon Nanocrystals. *Phys. Rev. B* **2005**, *72*, 075423.
37. Ramos, L.; Weissker, H.; Furthmuller, J.; Bechstedt, F. Optical Properties of Si and Ge Nanocrystals: Parameter-free Calculations. *Phys. Status Solidi B* **2005**, *242*, 3053.
38. Hybertsen, M. S. Absorption and Emission of Light in Nanoscale Silicon Structures. *Phys. Rev. Lett.* **1994**, *72*, 1514.
39. Kovalev, D.; Heckler, H.; Ben-Chorin, M.; Polisski, G.; Schwartzkopff, M.; Koch, F. Breakdown of the *k*-Conservation Rule in Si Nanocrystals. *Phys. Rev. Lett.* **1998**, *81*, 2803–2806.
40. Sykora, M.; Mangolini, L.; Schaller, R. D.; Kortshagen, U.; Jurbergs, D.; Klimov, V. I. Size-Dependent Intrinsic Radiative Decay Rates of Silicon Nanocrystals at Large Confinement Energies. *Phys. Rev. Lett.* **2008**, *100*, 067401.
41. Zhou, Z.; Brus, L.; Friesner, R. Electronic Structure and Luminescence of 1.1-and 1.4-nm Silicon Nanocrystals: Oxide Shell *versus* Hydrogen Passivation. *Nano Lett.* **2003**, *3*, 163–167.
42. Dexter, D. L. *Solid State Physics*; Academic, New York, 1958; Vol. 6, pp 358−361.
43. Califano, M.; Franceschetti, A.; Zunger, A. Temperature Dependence of Excitonic Radiative Decay in CdSe Quantum Dots: the Role of Surface Hole Traps. *Nano Lett* **2005**, *5*, 2360–2364.
44. Wilson, W. L; Szajowski, P. F.; Brus, L. E Quantum Confinement in Size-Selected, Surface-Oxidized Silicon Nanocrystals. *Science* **1993**, *262*, 1242–1244.
45. Brus, L. E.; Szajowski, P. F.; Wilson, W. L.; Harris, T. D.; Schuppler, S.; Citrin, P. H. Electronic Spectroscopy and Photophysics of Si Nanocrystals: Relationship to Bulk c-Si and Porous Si. *J. Am. Chem. Soc.* **1995**, *117*, 2915–2922.

46. Chelikowsky, J. R.; Troullier, N.; Saad, Y. Finite-Difference-Pseudopotential Method: Electronic Structure Calculations without a Basis. *Phys. Rev. Lett.* **1994**, *72*, 1240–1243.
47. Kronik, L.; Makmal, A.; Tiago, M. L.; Alemany, M. M. G.; Jain, M.; Huang, X.; Saad, Y.; Chelikowsky, J. R. PARSEC-the Pseudopotential Algorithm for Real-Space Electronic Structure Calculations: Recent Advances and Novel Applications to Nano-structures. *Phys. Status Solidi B* **2006**, *243*, 1063–1079.
48. Information regarding PARSEC and RGWBS can be obtained at http://parsec.ices.utexas.edu/ and http://users.ices.utexas.edu/mtiago/RGWBS/manual.html, respectively.